PERGAMON

International Journal of Solids and Structures 40 (2003) 1139–1164

INTERNATIONAL JOURNAL OF SOLIDS and STRUCTURES

www.elsevier.com/locate/ijsolstr

A failure criterion for fiber reinforced polymer composites under combined compression–torsion loading

Chandra S. Yerramalli, Anthony M. Waas *

Composite Structures Laboratory, Department of Aerospace Engineering, University of Michigan, Ann Arbor, MI 48109-2118, USA

Received 14 March 2002; received in revised form 5 November 2002

Abstract

A fracture mechanics based failure criterion for unidirectional composites under combined loading has been developed. The predictions from this criterion have been compared with experimental data obtained from combined compression–torsion loading of glass and carbon fiber reinforced polymer composites of 50% fiber volume fraction. The specimens were loaded under rotation control and displacement control in a proportional manner. Comparison of the Budiansky–Fleck kinking model, specialized to a solid circular cylinder, and the new failure model against experimental data suggests that the Budiansky–Fleck model predictions do not capture the variation of compressive strength as a function of shear stress for glass fiber composites. This is because these composites fail predominantly by compressive splitting. The Budiansky–Fleck model predictions are appropriate for composites that fail by compressive kinking. The new model predictions capture the experimental results for glass composites where the compression strength is initially unaffected by shear stress but undergoes a drastic reduction when a critical value of shear stress is reached.

Keywords: Compression; Combined compression torsion; Composites; Fracture; Kinking; Splitting; Failure mechanisms

1. Introduction

The compressive strength of fiber reinforced polymer matrix composites (FRPC) has been a limiting design feature in the use of FRPC as a primary structural member. Beginning with the work by Rosen (1965), who modeled the fiber composites as a layered plate material undergoing elastic buckling, a significant amount of insight into the compressive behavior of composites has been gained by a combination of experiments and analytical modeling. The existing literature in the area of compressive behavior of FRPC can be broadly divided into two areas based on the failure mechanism being investigated. The first is the microbuckling of fibers in an inelastic matrix leading to kinking of fibers under the action of pure compression loading and another is the splitting failure of composites. The splitting failure mode in glass composites has been reported by Piggott (1981), Piggott and Harris (1980), Lee and Waas (1999) and Oguni

* Corresponding author. Tel.: +1-734-764-8227; fax: +1-734-763-0578.
E-mail addresses: chandu@engin.umich.edu (C.S. Yerramalli), dcw@umich.edu (A.M. Waas).

0020-7683/02/$ - see front matter © 2002 Elsevier Science Ltd. All rights reserved.
doi:10.1016/S0020-7683(02)00649-2

and Ravichandran (2000). Splitting is a distinctly different failure mechanism from kinking. This mechanism, like kinking, is found to be a compressive strength limiting feature in glass composites. Lee and Waas (1999), and independently, Oguni and Ravichandran (2000) developed fracture mechanics based failure models for predicting the compressive splitting strength of FRPC. Compressive splitting has also been observed in other brittle materials like rock and certain classes of ceramics (Nemat-Nasser and Horii, 1982; Nemat-Nasser and Deng, 1994). Splitting failure in these materials have been modeled by appealing to ideas of fracture mechanics, for example, the wing–crack model (Horii and Nemat-Nasser, 1985, 1986).

In FRPC, compared to splitting, the kinking failure mode has been studied exhaustively through experiment and analytical/numerical modeling (Argon, 1972; Budiansky, 1983; Fleck et al., 1995; Kyriakides et al., 1995; Fleck, 1997; Vogler and Kyriakides, 1999; Hsu et al., 1999; Vogler and Kyriakides 2001). Argon (1972) and later Budiansky (1983) were the first to develop models for kinking failure in composites. They observed that the fibers in a unidirectional fiber reinforced composite are not perfectly straight. Owing to this, they reasoned that fiber mislignments cause the development of local shear stresses in the composite under the action of remote pure compressive loads. When these shear stresses exceed the value of the shear yield stress of the matrix the fibers undergo shear buckling leading to failure in compression. Later Budiansky and Fleck (1993) extended the above ideas to include the effect of matrix strain hardening on the compressive strength of fiber composites. Similarly, the effect of strain gradients on compressive strength of carbon fiber composites has been investigated and reported in Wisnom and Atkinson (1997) and Drapier et al. (2001). Recently, the possibility of kinking initiating due to internal fiber breaks has been given consideration by Narayanan and Schadler (1999). A survey of the literature on compressive failure can be referred to in the review paper by Waas and Schultheisz (1996) and a more recent one on the various compressive strength models by Naik and Kumar (1999). Based on previous research it can be inferred that the compression strength of polymer composites depends on the fiber mechanical properties, matrix shear properties, fiber/matrix interface fracture energy, fiber volume fraction, V_f, and initial misalignment of fibers. Understanding the effect of each of these parameters on the observed compressive strength and the mode of failure is very important if a proper understanding of the compressive behavior of composites is to be attained. Of the above parameters, induced local shearing stresses governed by the response of the matrix in shear and the interfacial fracture energy of the composite play an important role in determining the failure mechanism and the failure strength of the composite.

The presence of shearing stresses, during the application of compressive loads on the specimen, induces misalignments in the fibers which would degrade the performance of the composite under compressive loads. Thus, combined axial/torsional loading of solid cylindrical specimens will help in understanding the effect of shear on the composite compressive strength in a systematic manner. Relatively few experimental results are available for the combined compression–shear loading of polymer matrix composites. Jelf and Fleck (1994) conducted tests on hollow composite tubes made of carbon/epoxy with a fiber volume fraction, V_f of 65%. A constant value of shearing stress was applied to the tubes, after which the compression load was increased until failure. They found that the composite compressive strength decreased linearly with increasing values of remotely applied shear stress. Even though a cylindrical tube is an ideal geometry to study the response of composite materials under combined compression/shear loading, the manufacturing of the walled tubular specimens of FRPC results in specimen behavior that may not be representative of FRPC bulk behavior. Studies on the effect of shear on composite compressive strength were also reported in Vogler et al. (2000) and Vogler and Kyriakides (2001). Tests were conducted on flat coupons of AS4/PEEK composites with a specially prepared test bed to apply shearing stresses and compression stresses simultaneously. These studies reported that the compression strength of AS4/PEEK specimens dropped in a linear manner with increasing values of remotely applied shear stresses. Vogler et al. (2000) performed finite element analysis of AS4/PEEK under combined compression and shear loading to compare with the experimental work. These previous investigations on the effect of combined loading on compressive strength have been restricted to carbon composites at fixed fiber volume fraction, V_f, and under non-proportional

remote loading. The focus of these studies was the effect of shear on altering the details of kinking. The present study, on the other hand is focussed on understanding how various parameters influence the mode of failure under combined loading. To do this, we have chosen to examine the behavior of solid cylindrical specimens of glass fiber/vinylester and carbon fiber/vinylester unidirectional composites at a fixed fiber volume fraction of $V_f = 50\%$ when subjected to proportional compressive/shear loading.

The paper is organized as follows. Experimental details and results pertaining to the combined compression–torsion experiments are presented first followed by an extension of the Budiansky–Fleck model to a solid circular cylindrical configuration. This analysis is followed by the introduction of a new splitting model appropriate for combined loading. This new model is an extension of the earlier work by Lee and Waas (1999). This is followed by a discussion and comparison of the experimental results with model predictions. Finally, concluding remarks are offered.

2. Experimental details

Solid cylindrical specimens of $V_f = 50\%$ were manufactured using an in-house composite manufacturing facility. Composites were made using both E-glass (Vetrotex-certainteed) fibers of 24.1 μm diameter and IM-7-12K carbon fibers (Hexcel) of 5 μm diameter with vinylester resin (Dow Derakane 411-C50). The specimens were cut with a fine diamond tip saw using a low speed cutting machine into lengths of 63.5 mm. The gage length of the specimen was about 12.6 mm and the average diameter of the specimen was 6.7 mm. The specimens were subjected to pure compression, pure torsion and combined compression–torsion under displacement control loading, rotation control loading and combined displacement–rotational control loading, respectively. The tests were performed on an axial–torsional MTS machine which had the capacity to simultaneously apply axial and torsional loads. The strains in the specimens were measured by attaching three strain gages on the specimen surface, two along the axial direction on opposite surfaces and the third one at an angle of 45° to the vertical. The third strain gage was used to calculate the shearing strain and the two strain gages along the generators of the cylindrical specimen were used to measure the axial strain in the specimen. Apart from the strain gage data, data was collected on the cross head displacement, cross head rotation, axial force and the torque acting on the specimen. As has been reported in the literature (Martinez et al., 1981; Vogler and Kyriakides, 1999), the type of gripping influences the failure strength of the fiber reinforced polymer composite under compression. As can be seen in Fig. 1 the rectangular block grips provide uniform continuous contact with the sides of the specimen. In contrast, the collet grips have some grooves to improve gripping in torsion, which leads to non-uniform discontinuous contact. Pure compression tests were done using the block grips along with the setup shown in Fig. 2 which resulted in a slightly lower compressive strength. We observed that the initiation of kink bands in the carbon fiber composites occurred inside the grips. The use of collet grips resulted in a higher compressive strength. For the combined compression-torsion tests it is required that the specimen be gripped in such a manner that there is no slip between the specimen surface and the interior of the grip, while rotating the specimen and simultaneously applying an axial load. The grooves in the collet grips provide the above functionality. Hence, collet grips were used along with an adapter to mount onto the MTS cross head.

2.1. Testing plan

Initially pure compression and pure torsion tests were performed on the composite specimens, which correspond to the vertical and horizontal axis of the loading diagram as shown in Fig. 3. The pure compression tests were performed under displacement control at a uniform cross head displacement of 0.0381 mm/s and the pure torsion tests were performed at a uniform cross head rotation of 0.0635°/min. As

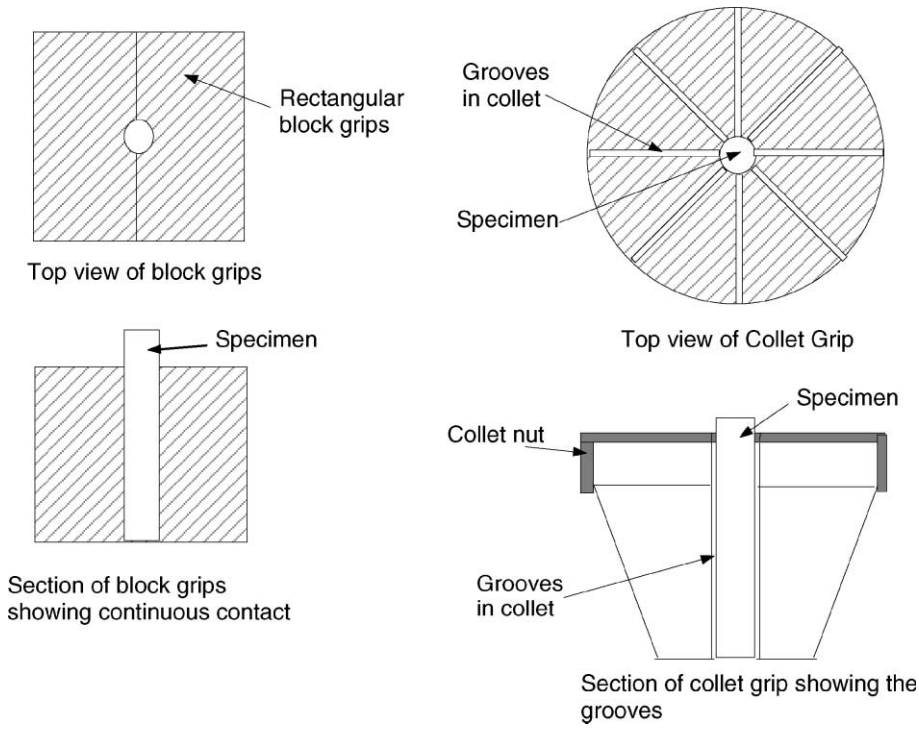

Fig. 1. Grip cross-sections.

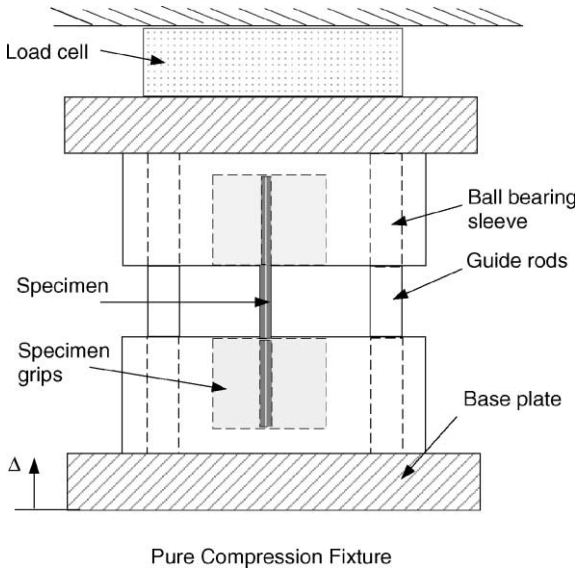

Fig. 2. Pure compression test setup.

can be seen in Fig. 3 different loading paths were adopted and the failure mechanism and failure strength in each case was noted. The loading ratio was defined in terms of the axial displacement and the arc dis-

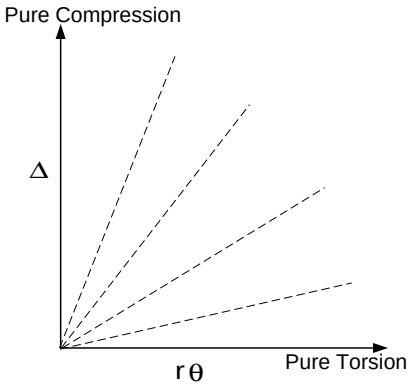

Fig. 3. Different loading paths in a displacement/rotation control test.

placement as $\frac{\Delta}{R\theta}$, where Δ is the axial cross head displacement, θ is the applied cross head rotation and R is the radius of specimen. This was repeated for both glass and carbon composites.

2.2. Experimental results

In this section, important features of the experimental results will be presented. The combined compression–torsion loading of solid cylindrical specimens of glass and carbon fiber composites was done under displacement and rotational control. Fig. 4 shows the proportional loading for a glass/vinylester composite specimen with $\Delta/r\theta = 5.23$ as sensed by the strain gages in the gage section of the specimen. For this type of loading ratio, Fig. 5 shows the plot of axial stress as a function of shear stress. It can be seen that the curve

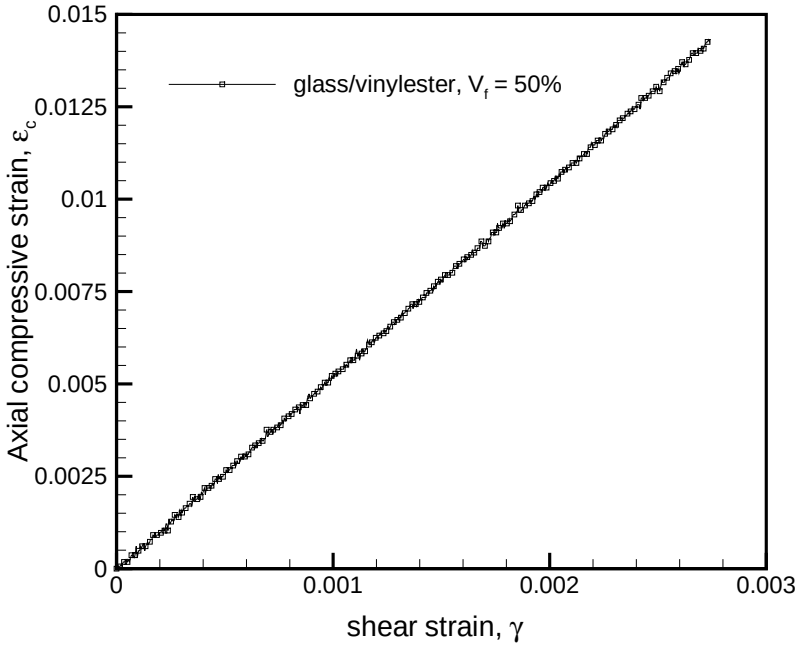

Fig. 4. Axial strain as a function of shear strain for $\Delta/r\theta = 5.23$ and glass/vinlyester composite.

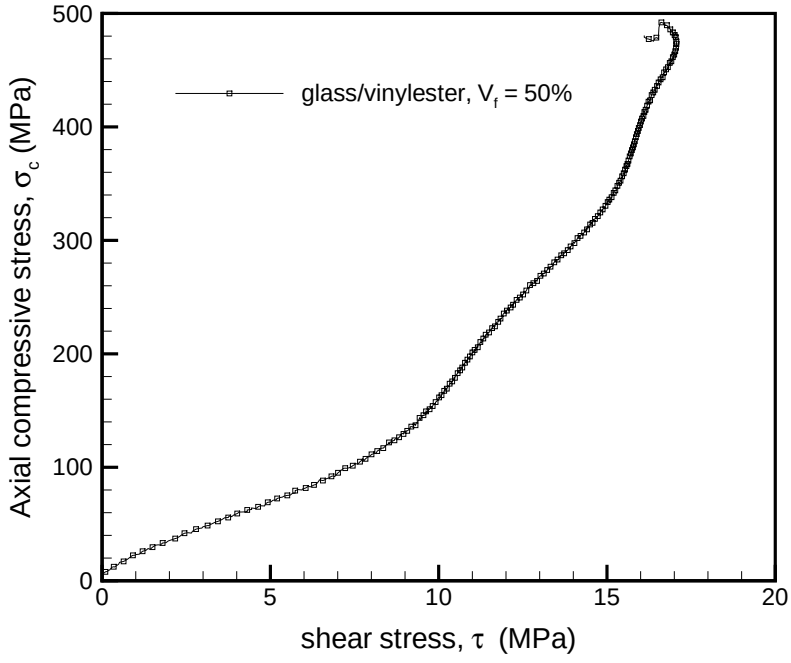

Fig. 5. Axial stress vs shear stress for $\Delta/r\theta = 5.23$ and glass/vinylester composite.

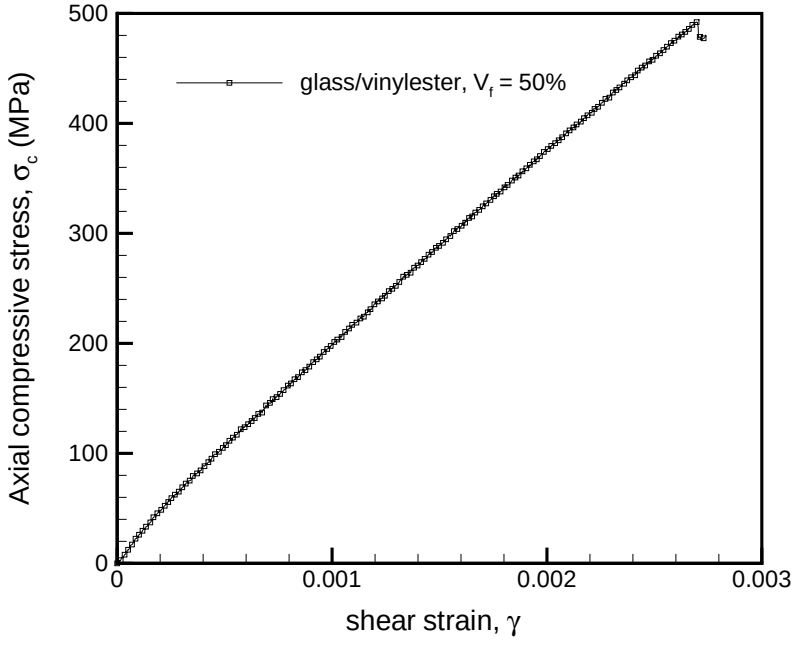

Fig. 6. Axial stress variation with applied shear strain for $\Delta/r\theta = 5.23$ and glass/vinylester composite.

is non-linear except at the initial stages of loading. The linear variation of axial stress with shear strain for the same specimen is shown in Fig. 6. Hence, it can be inferred that the non-linear nature of the axial stress-

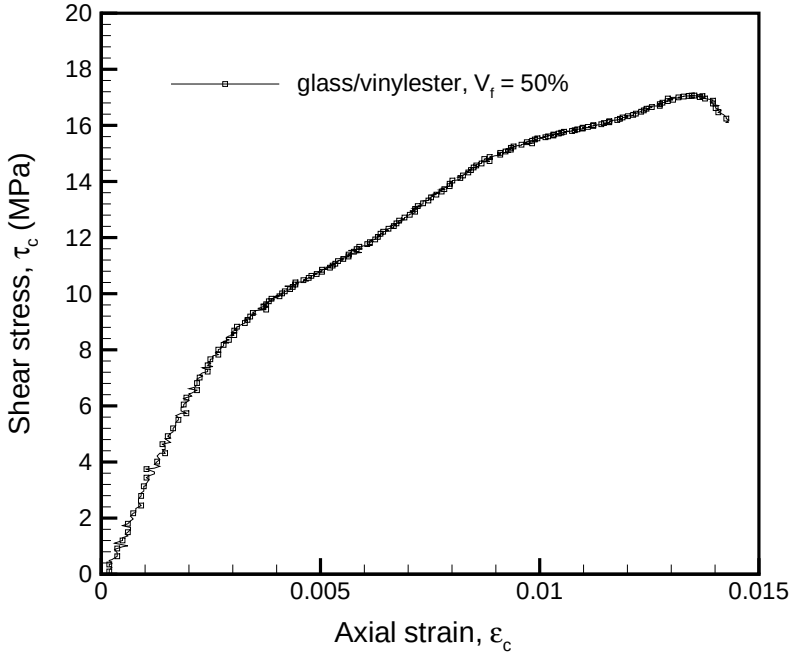

Fig. 7. Shear stress variation with applied axial strain for $\Delta/r\theta = 5.23$ and glass/vinylester composite.

shear stress curve is because of the non-linearity induced by the shear response of the composite. This can be seen in Fig. 7 where the shear stress is plotted as a function of the axial strain. A plot showing the failure envelope of glass/vinylester and carbon/vinylester composites are shown in Figs. 8 and 9.

An important observation that can be made from the experimental data of the combined loading tests of glass/vinylester and carbon/vinylester composite specimens is the distinct difference in both the response to remote shear stress, and in the failure mechanisms. It was found that the glass composites failed by a combination of splitting and kinking at high values of $\Delta/r\theta$. The splitting failure of glass composites is usually characterized by extensive brooming of fibers in the split region as indicated in Fig. 11. Fig. 12 is a high resolution SEM micrograph of a longitudinal section in the splitting region of the glass composite. It can be seen from the SEM pictures that there is extensive fiber/matrix debonding and fiber breakage. Whereas, at lower values of $\Delta/r\theta = (0.4 - 0.6)$ the failure was by kinking and is shown in Fig. 13. These observations are similar to those made by Piggott and Harris (1980) in which they found the failure mode changing from kinking/splitting to kinking as the matrix became softer. In their work they used a matrix material with different curing times to obtain a range of matrix stiffness and yield stress values for the matrix. The present work indicates that the effect of remote shear stress beyond the shear yield stress is similar to that of a partially cured matrix. Thus, matrix stiffness and matrix yield stress are important parameters in determining the failure mechanism. The failed glass composite specimens were cross-sectioned and observed under SEM to study the failure mode. Figs. 11 and 13 show that there is a change in failure mode as the shear stress at failure exceeds the shear yield stress of the composite i.e. as the $\Delta/r\theta$ value becomes low.

Carbon composites, however, failed by kinking as seen in Fig. 14, throughout the range of loading ratios for which the tests were conducted. These experimental findings indicate the importance of constructing a failure model that can capture different and distinct failure mechanisms. Clearly, kinking is not the only strength limiting mechanism of failure. Our intent in the next section is to establish analytical models for

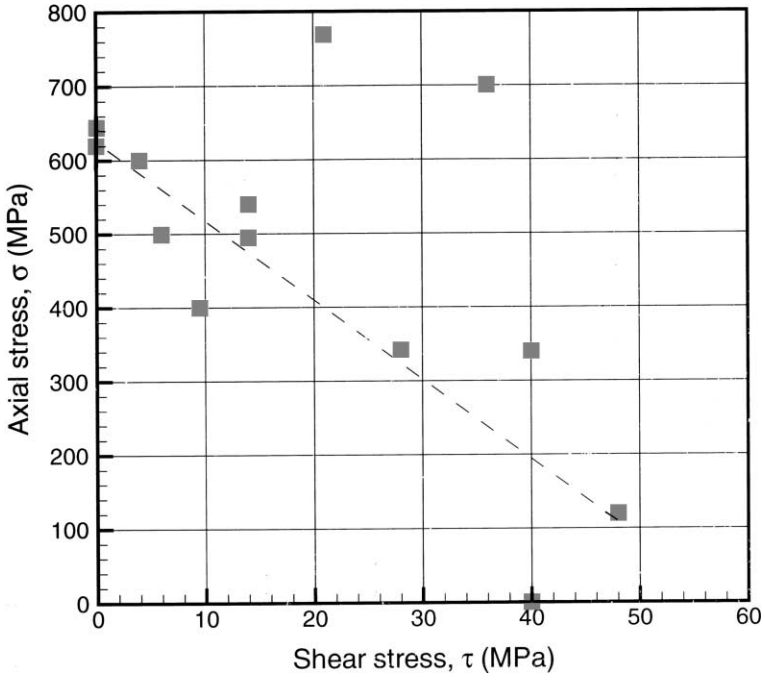

Fig. 8. Failure envelope for a carbon/vinylester composite of $V_f = 50\%$.

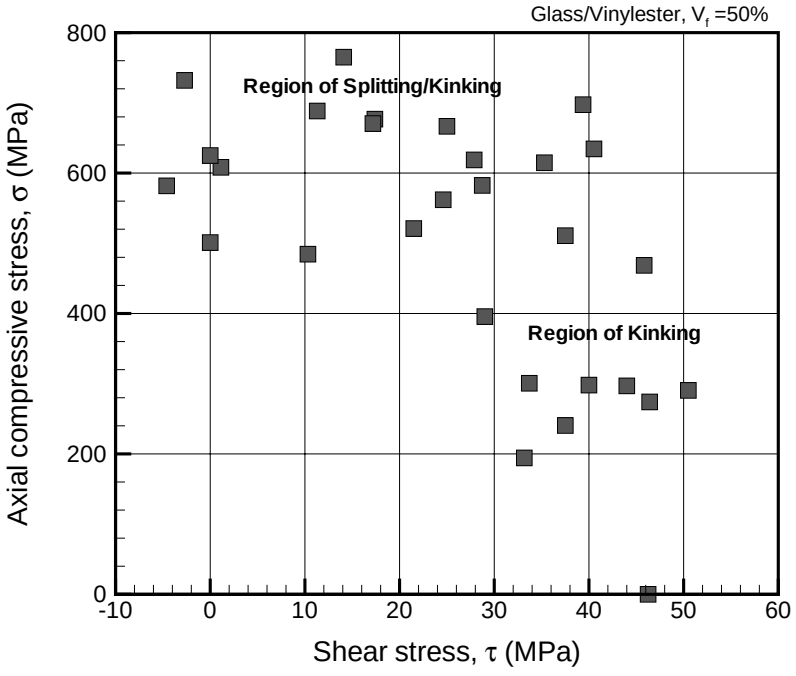

Fig. 9. Failure envelope for a glass/vinylester composite of $V_f = 50\%$.

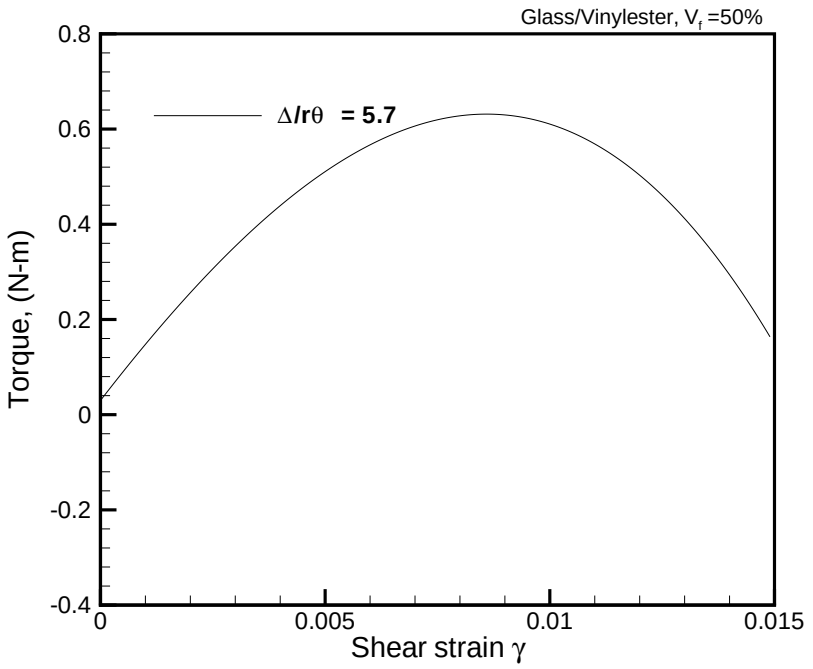

Fig. 10. Plot showing the stress reversal in glass composite for high values of $\Delta/r\theta$.

kinking and splitting with a view to understanding which parameters influence the different mechanisms of failure.

Some other observations that were made from the experiments are as follows. For high values of $\Delta/r\theta$, the compressive strength of some specimens were found to increase. This could be due to the fact that for small rotations of cross-sections, the applied shear strain acts in a manner to reduce the misalignments thus leading to an increase in compressive failure strength. Further, for high values of $\Delta/r\theta$ (which implies high compression and low rotation) torque reversal was observed. This can be seen in Fig. 10, where the torque undergoes a change in sign. This can be attributed to the result of the interaction between the induced shear strain caused by the applied axial compression and the sense of the shear strain due to the applied end rotation. In cases of high $\Delta/r\theta$, the induced shear strain must be higher than the applied shear (due to rotation) causing the relaxation in torque sensed by the torsional load cell. In a load control experiment this could lead to an instability in torsion, which was the primary reason for conducting the present experiments under displacement and rotation control.

3. Analysis

The modified Budiansky–Fleck (MBF) model for kinking failure in solid composite cylinders under combined compression–torsion loading is presented, followed by a novel energy based splitting failure model in pure compression, pure torsion and combined compression–torsional loading.

3.1. Kinking analysis

The Budiansky–Fleck model is based on the assumption that the shear stress variation is a known function of the radius of the specimen. However, in case of solid cylindrical specimens the shear stress

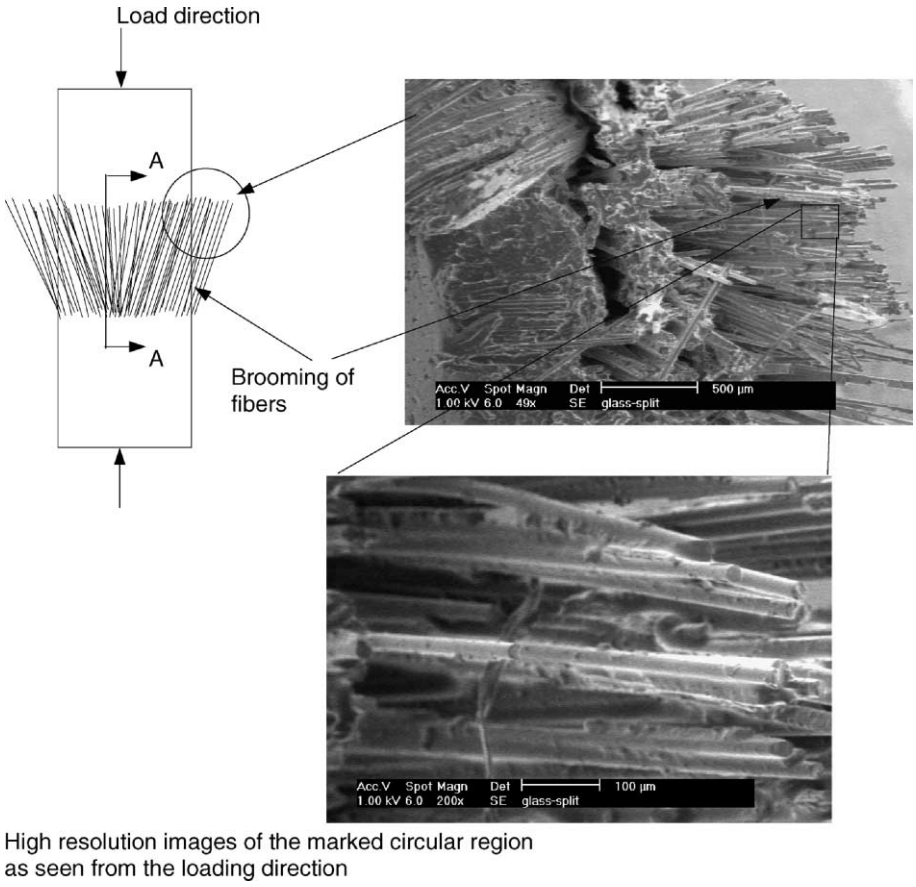

Fig. 11. Typical image of a split region in glass composites with extensive brooming of fibers.

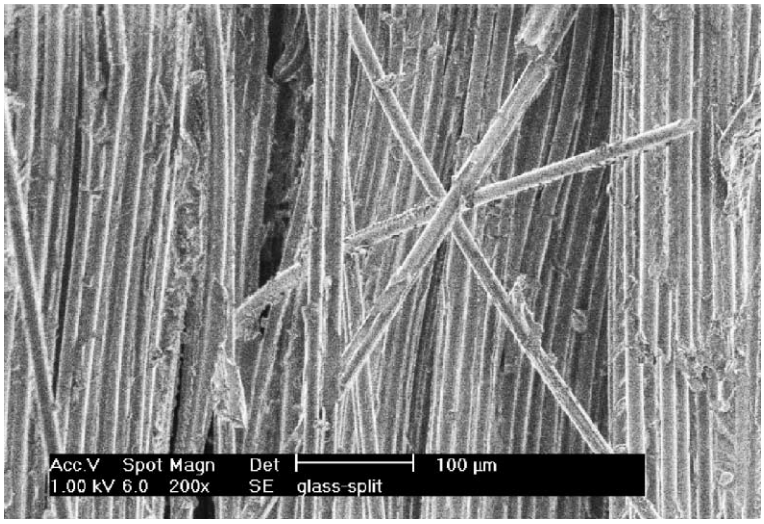

Fig. 12. Image at the cross-section A–A of the splitting zone in a glass composite, $V_f = 50\%$.

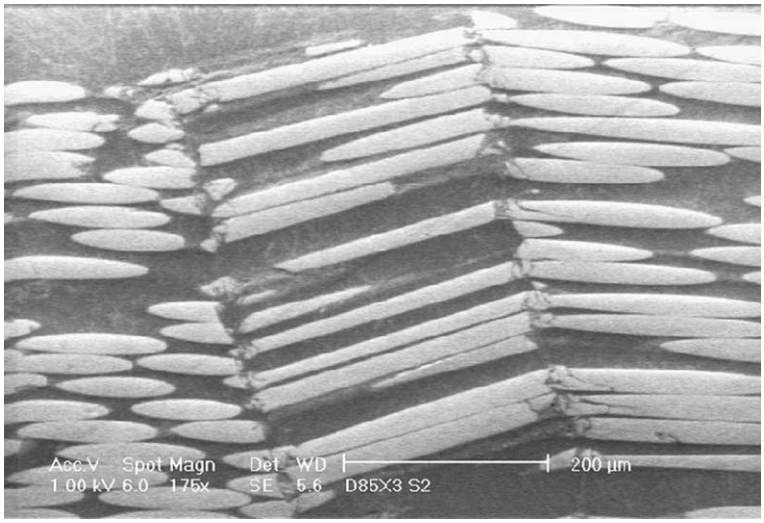

Fig. 13. Kinking failure in glass composites at $\Delta/r\theta = 0.59$.

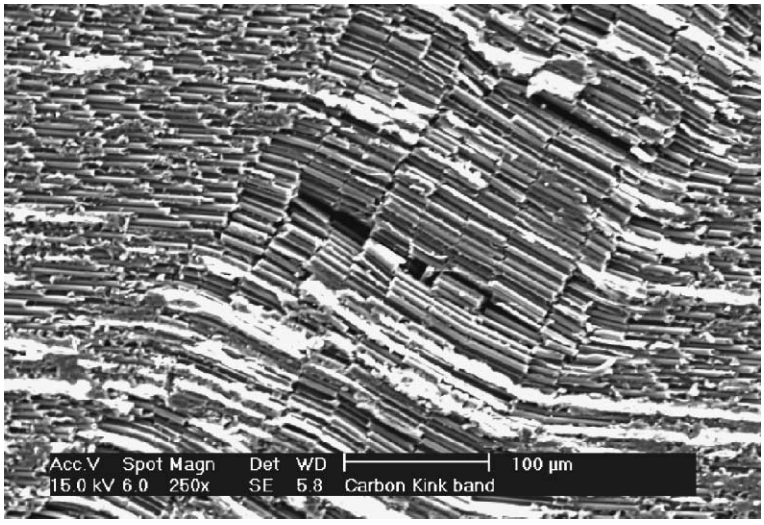

Fig. 14. Kinking failure in carbon composites.

distribution is not a known function of the radius. Hence, the current formulation of Budiansky–Fleck model was modified to apply it to the case of solid cylindrical specimens. For solid cylindrical specimens, under pure torsion, Lyon (1991) who extended the work of Nadai (1950), has shown that the expression for the shear stress τ_R at radius, $r = R$ in terms of the applied torque, T and the rotation θ is as given below in Eq. (1)

$$\tau_R = \frac{3}{2\pi R^3}\left[T + \frac{\theta}{3}\frac{\mathrm{d}T}{\mathrm{d}\theta}\right] \tag{1}$$

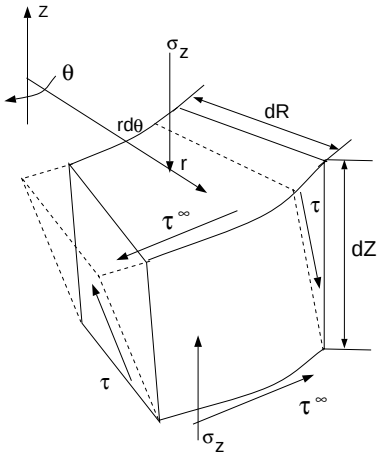

Fig. 15. Free body diagram of a kinked segment of a cylinder under combined compression and torsion.

The expression for critical compressive stress in the presence of remotely applied shear stress, τ^{∞} is derived for a zero angle kink band as follows. As shown in Fig. 15, the free body diagram of a small segment at a distance r from the center of the cylindrical specimen is considered in the deformed configuration with a uniform axial stress σ_Z acting along the Z-direction. Then, taking a balance of moments on this segment, one obtains the following expression for axial stress in terms of the remote shear stress, τ^{∞}, the shearing response of the composite material, $\tau(r)$, within an element of kinked fibers, the initial misalignment angle of the fibers, ϕ, and the applied shear strain, $\gamma(r)$

$$\sigma_z = \frac{\tau(r) - \tau^{\infty}}{\phi + \gamma(r)} \tag{2}$$

In the case of solid specimens, the shear stress $\tau(r)$ is not a linear function of r, hence its variation with r is unknown and cannot be evaluated. However, the variation of shear stress, $\tau(r)$ is known as a function of shear strain, γ, which is a linear function of r given by $r\theta/l$, where θ is the rotation and l is the specimen gage length. Therefore the first step in developing the MBF is to express the shear stress as a function of shear strain, γ. This is achieved by expressing the specimen radius r as $\frac{\gamma l}{\theta}$. Using the above substitution for r and multiplying both sides of Eq. (2) by $r^2 \mathrm{d}r\,\mathrm{d}\theta$ and integrating, we can write Eq. (2) as

$$\int_0^{2\pi}\int_0^{\gamma_R} \sigma_z(\phi+\gamma)\frac{\gamma^2}{v^3}\,\mathrm{d}\gamma\,\mathrm{d}\theta = \int_0^{2\pi}\int_0^{\gamma_R} \tau(\gamma)\frac{\gamma^2}{v^3}\,\mathrm{d}\gamma\,\mathrm{d}\theta - \int_0^{2\pi}\int_0^{\gamma_R} \tau^{\infty} r^2\,\mathrm{d}r\,\mathrm{d}\theta \tag{3}$$

where v is twist per unit length, θ/l. Simplifying the above equation, we obtain the following expression for average critical compressive stress, σ_z, where, we substitute T the applied torque for $\int_0^{2\pi}\int_0^{R} \tau^{\infty} r^2\,\mathrm{d}r\,\mathrm{d}\theta$ and γ_R for shear strain at $r = R$. Then,

$$\sigma_z = \frac{\frac{1}{\gamma_R^3}\int_0^{\gamma_R} \tau(\gamma)\gamma^2\,\mathrm{d}\gamma - \frac{T}{2\pi R^3}}{\frac{\phi}{3} + \frac{\gamma_R}{4}} \tag{4}$$

The integral term in (4) represents the shear response of the composite material and can be obtained from a pure torsion test of the composite with similar fiber volume fraction. In Eq. (4), if we substitute $\alpha\sigma_z$ for $\frac{T}{2\pi R^3}$, where α is the loading ratio, then we obtain an expression for σ_z in terms of the shear response of the composite, loading ratio, α, the misalignment angle, ϕ, and the induced shear strain, γ_R at $r = R$, as given

below in Eq. (5). On solving equation (5) we get a limit load for σ_z at some value of γ. This represents the critical kinking compressive stress for the composite

$$\sigma_z = \frac{\frac{1}{\gamma_R^3}\int_0^{\gamma_R} \tau(\gamma)\gamma^2 \, d\gamma}{\alpha + \frac{\phi}{3} + \frac{\gamma_R}{4}} \tag{5}$$

3.2. Splitting analysis

Splitting failure mode has been observed in glass composites by Piggott (1981), Lee and Waas (1999) and Oguni and Ravichandran (2000). The micrographs of the failed specimens as seen in Figs. 11 and 12 reveal that the fiber/matrix interfaces split during failure and the fibers are broken. Some of the fibers in the region of splitting actually show the matrix attached to the fiber surface. This indicates that the splitting failure does not always happen along the interface but sometimes meanders into the matrix region away from the fiber/matrix interface. In high fiber volume fractions (0.4–0.6), kink bands are also observed along with the fiber/matrix splitting failure cracks in glass composites. However, for the glass composites tested isolated kink bands were never formed as observed in carbon composites. Based on these observations Lee and Waas (1999) developed a energy based splitting failure model. In following sections, we have extended the splitting model of Lee and Waas (1999) for pure compression to the case of pure torsion and combined compression–torsion. For the sake of completeness, all three derivations are presented.

3.2.1. Strain energy release rate, $\mathcal{G}$

Consider a representative volume element (RVE) of the composite, consisting of a concentric cylinder of fiber and matrix, with a fiber radius, r_0 and an outer region of matrix with radius, r_1, and subjected to a external axial load, P and torque, T, as shown in Fig. 16. Following the methodology of the composite

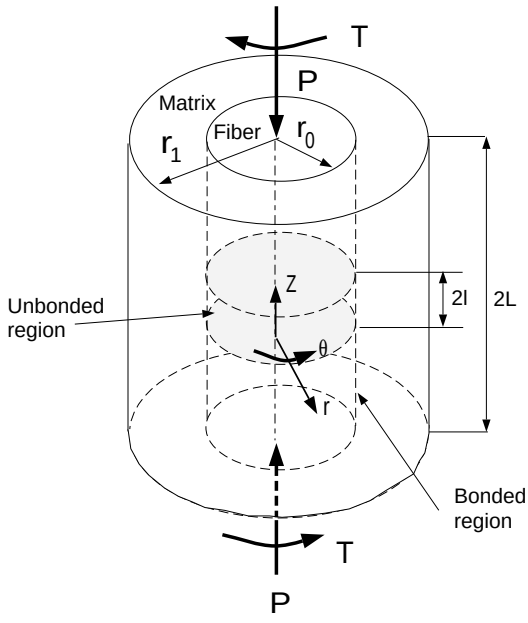

Fig. 16. Composite cylinder under compression–torsion loading.

cylinder model (CCM) as given in the text by Christensen (1991), we assume the composite to be consisting of a collection of such RVEs. The outer radius of matrix in the RVE is chosen to satisfy the fiber volume fraction requirement such that $r_1^2 = V_f/r_0^2$. The outer matrix surface ($r = r_1$) is assumed to be traction free. The height of the cylinder is taken to be $2L$ with a interfacial crack of $2l$ embedded at the interface of fiber and matrix. The composite is assumed to have perfect bonding outside the crack region ($l \leqslant z \leqslant L$) and ($-L \leqslant z \leqslant -l$). The total potential energy is written as $\Pi = U - W$, where U is the strain energy stored in the composite cylinder and W is the work done by the external forces.

3.2.2. Axial loading

The expression for strain energy release rate (SERR), $\mathscr{G}_{\text{axial}}$ is derived below. The material is assumed to behave as a linear elastic material under the action of externally applied axial load, P. The strain energy release rate, $\mathscr{G}$ is defined as follows $\mathscr{G} = -\frac{\mathrm{d}\Pi}{\mathrm{d}\Delta}$. The crack surface area, A is taken to be $4\pi r_0 l$. Hence, the expression for strain energy release rate can be written as $\mathscr{G} = \frac{-1}{4\pi r_0}\frac{\mathrm{d}\Pi}{\mathrm{d}l}$.

The total potential energy in the case of displacement control loading (the applied displacement, Δ, is held fixed during crack propagation) is

$$\Pi = U - W, \quad U = \frac{1}{2}P\Delta \quad \text{and} \quad W = 0$$

$$\mathscr{G} = -\frac{\Delta}{8\pi r_0}\frac{\mathrm{d}P}{\mathrm{d}l}$$

Using the definition of compliance, $c = \Delta/P$, we obtain

$$\frac{\mathrm{d}P}{\mathrm{d}l} = -\frac{P^2}{\Delta}\frac{\mathrm{d}c}{\mathrm{d}l} \quad \text{Hence,} \quad \mathscr{G} = \frac{P^2}{8\pi r_0}\frac{\mathrm{d}c}{\mathrm{d}l} \tag{6}$$

For load control (the applied load, P, is held fixed in magnitude during crack propagation), we get

$$\Pi = U - W, \quad U = \frac{1}{2}P\Delta \quad \text{and} \quad W = P\Delta$$

$$\mathscr{G} = \frac{P}{8\pi r_0}\frac{\mathrm{d}\Delta}{\mathrm{d}l}$$

Using the definition of compliance, $c = \Delta/P$, we obtain

$$\frac{\mathrm{d}\Delta}{\mathrm{d}l} = P\frac{\mathrm{d}c}{\mathrm{d}l} \quad \text{Hence,} \quad \mathscr{G} = \frac{P^2}{8\pi r_0}\frac{\mathrm{d}c}{\mathrm{d}l} \tag{7}$$

Note that the expression for strain energy release rate, $\mathscr{G}$, is same under load control as well as displacement control loading due to the assumption of linear elastic material behavior.

For the cracked region in Fig. 16 ($-l \leqslant z \leqslant l$), the stress state which corresponds to axial compression is given as follows from Hyer and Waas (2000).

Fiber

$$\sigma_z = \frac{PE_f}{\pi r_0^2 \delta}$$

Matrix

$$\sigma_z = \frac{PE_m}{\pi r_0^2 \delta}$$

where

$$\delta = E_{\mathrm{f}} + E_{\mathrm{m}}\left(\frac{1}{V_{\mathrm{f}}} - 1\right)$$

All other stresses are zero.

The axial contraction of the fiber and matrix can be obtained from the axial strain corresponding to the above stresses, and is given by

$$\Delta_1 = \int_{-l}^{l} \epsilon_z \, \mathrm{d}z = \frac{2Pl}{\pi r_0^2 \delta}$$

For the uncracked region in Fig. 16 ($l \leqslant z \leqslant L, -L \leqslant z \leqslant -l$), the stress state which is three dimensional, is given as follows from Hyer and Waas (2000),

Fiber

$$\sigma_r = \sigma_\theta = \frac{2P}{\pi r_0^2}\alpha\beta(v_{\mathrm{f}} - v_{\mathrm{m}})(V_{\mathrm{f}}^{-1} - 1)$$

$$\sigma_z = \frac{\beta P}{\pi r_0^2}\left[E_{\mathrm{f}} + 4\alpha v_{\mathrm{f}}(v_{\mathrm{f}} - v_{\mathrm{m}})(V_{\mathrm{f}}^{-1} - 1)\right]$$

Matrix

$$\sigma_r = 2\alpha\beta P\frac{v_{\mathrm{f}} - v_{\mathrm{m}}}{\pi r_0^2}\left(\frac{r_0^2}{r^2 V_{\mathrm{f}}} - 1\right)$$

$$\sigma_\theta = -2\alpha\beta P\frac{v_{\mathrm{f}} - v_{\mathrm{m}}}{\pi r_0^2}\left(\frac{r_0^2}{r^2 V_{\mathrm{f}}} + 1\right)$$

$$\sigma_z = \frac{\beta P}{\pi r_0^2}\left[E_{\mathrm{m}} - 4\alpha v_{\mathrm{m}}(v_{\mathrm{f}} - v_{\mathrm{m}})\right]$$

where

$$\alpha = \left[\frac{2(1 + v_{\mathrm{f}})(1 - 2v_{\mathrm{f}})}{E_{\mathrm{f}}}(V_{\mathrm{f}}^{-1} - 1) + \frac{2(1 + v_{\mathrm{m}})(1 - 2v_{\mathrm{m}} + V_{\mathrm{f}}^{-1})}{E_{\mathrm{m}}}\right]^{-1}$$

$$\beta = \left[E_{\mathrm{f}} + (V_{\mathrm{f}}^{-1} - 1)\{E_{\mathrm{m}} + 4\alpha(v_{\mathrm{f}} - v_{\mathrm{m}})^2\}\right]^{-1}$$

The axial strains corresponding to these stresses are as follows.

Fiber

$$\epsilon_z = -\frac{v_{\mathrm{f}}}{E_{\mathrm{f}}}\sigma_r - \frac{v_{\mathrm{f}}}{E_{\mathrm{f}}}\sigma_\theta + \frac{1}{E_{\mathrm{f}}}\sigma_z = -\frac{4Pv_{\mathrm{f}}}{\pi r_0^2 E_{\mathrm{f}}}\alpha\beta(v_{\mathrm{f}} - v_{\mathrm{m}})(V_{\mathrm{f}}^{-1} - 1) + \frac{\beta P}{\pi r_0^2 E_{\mathrm{f}}}\left[E_{\mathrm{f}} + 4\alpha v_{\mathrm{f}}(v_{\mathrm{f}} - v_{\mathrm{m}})(V_{\mathrm{f}}^{-1} - 1)\right]$$

Matrix

$$\epsilon_z = \frac{4\alpha\beta P v_{\mathrm{m}}(v_{\mathrm{f}} - v_{\mathrm{m}})}{\pi r_0^2 E_{\mathrm{m}}} + \frac{\beta P}{\pi r_0^2 E_{\mathrm{m}}}\left[E_{\mathrm{m}} - 4\alpha v_{\mathrm{m}}(v_{\mathrm{f}} - v_{\mathrm{m}})\right]$$

The axial contraction of the fiber and matrix are the same and is given by

$$\Delta_2 = 2\int_{l}^{L} \epsilon_z \, \mathrm{d}z = \frac{2\beta P}{\pi r_0^2}(L - l)$$

Hence, the approximate total axial contraction, approximate compliance and change of compliance with respect to crack length, $\mathrm{d}c/\mathrm{d}l$ of the composite are as follows

$$\begin{aligned} \Delta &= \frac{2P}{\pi r_0^2}\left[\frac{l}{\delta}+\beta(L-l)\right] \\ c &= \frac{2}{\pi r_0^2}\left[\frac{l}{\delta}+\beta(L-l)\right] \\ \frac{\mathrm{d}c}{\mathrm{d}l} &= \frac{2}{\pi r_0^2}\left(\frac{1}{\delta}-\beta\right) \end{aligned} \tag{8}$$

In computing the above quantities, only the stress states of the cracked and uncracked regions are considered, whereas a region near the crack tip of finite size ϵ is not considered. In the present analysis, the above expression for $\mathrm{d}c/\mathrm{d}l$ is used, even though we have neglected the crack tip stress field in computing $\mathrm{d}c/\mathrm{d}l$. However, as explained later, for steady-state conditions, Eq. (8) is exact. In the region ϵ (Fig. 17), the stress state is influenced by the crack tip field. However, under steady-state conditions for self-similar crack growth, this region translates with the crack tip resulting in an increase of l and a corresponding decrease of $(L-l)$. Thus, while the axial contraction and compliance given by Δ and c above are approximate due to the negligence of the crack tip field, the rate of compliance change due to crack advancement, given by $\mathrm{d}c/\mathrm{d}l$ is exact, since the 'ϵ' region is invariant with respect to crack length. This fact enables us to calculate $\mathscr{G}$ accurately for steady state crack propagation. When the crack is small, initially the compliance change with respect to crack length, $\mathrm{d}c/\mathrm{d}l$, is dependent on the size of ϵ, but, as the crack length increases, $\mathrm{d}c/\mathrm{d}l$, becomes independent of crack length and attains the steady state value provided in Eq. (8). The derivation of $\mathrm{d}c/\mathrm{d}l$ including the dependence on ϵ is given in Yerramalli and Waas (2002a), for non-steady-state crack growth.

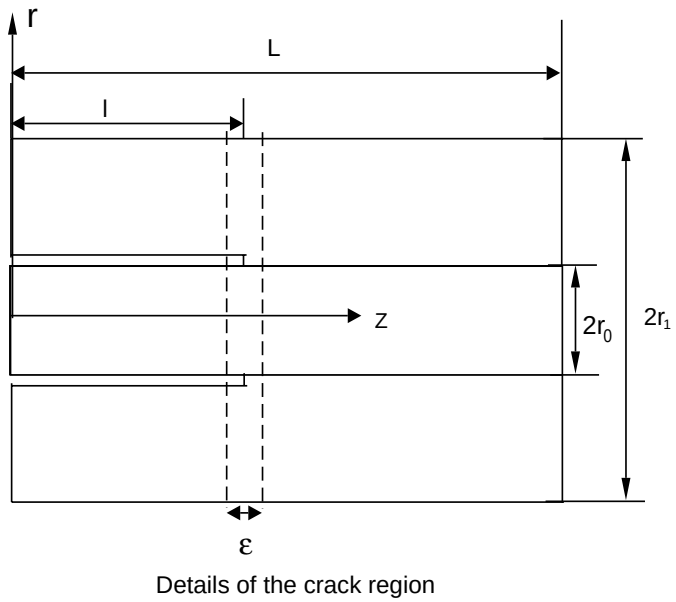

Fig. 17. Schematic cross-section of fiber–matrix cylinder showing the crack tip details.

From (8), the energy release rate per unit area is obtained as

$$\mathscr{G} = \frac{P^2}{4\pi^2 r_0^3}\left(\frac{1}{\delta} - \beta\right)$$

When $\mathscr{G}$, becomes equal to twice the critical interfacial fracture energy (γ_f) the initial crack propagates

$$\mathscr{G} = 2\gamma_f \tag{9}$$

Thus

$$\sigma_{cr} = \sqrt{\frac{8V_f^2\gamma_f}{r_0(1/\delta - \beta)}} \tag{10}$$

3.2.3. Misaligned fibers

The above analysis was developed for a perfectly aligned fiber. However, the fibers in a composite can have an initial misalignment with respect to the axial load. The expression for axial compliance for the case when the fiber is misaligned in the cracked region is presented in the current section. The axial compliance expression can be obtained by considering a slightly imperfect fiber with an initial imperfection of $w_0(x)$ and using kinematics that are appropriate for geometrically nonlinear beam theory as described in Appendix A. Then the relation between axial contraction Δ, and fiber load, P_f, can be obtained as

$$\frac{\Delta_1}{l} = \frac{-P_f}{A_f E_f}\left[1 + \frac{A_0^2 A_f}{2I_f}\right],$$

where A_f is the fiber cross-sectional area, I_f is the area moment of inertia and A_0 is the imperfection magnitude. From this relation an effective axial stiffness for the fiber is obtained and is given below

$$(EA)_{eff} = \frac{E_f A_f}{1 + \frac{A_0^2 A_f}{2I_f}},$$

Clearly, when the imperfection vanishes, one recovers the perfect fiber axial stiffness $(EA)_f$. In the present work, the imperfection amplitude is chosen to correspond to an initial misalignment angle of 2^0. A detailed derivation of the axial splitting model is presented in Lee and Waas (1999).

3.2.4. Torsional loading

Strain energy release rate expressions for a cylindrical specimen of linear elastic and non-linear elastic material under the action of pure torsion, T are developed below. Closed form expressions of the strain energy release rate for a linear elastic material are obtained in terms of the compliance of the material.

The strain energy release rate expression for a cylinder of radius r_0, under rotational (displacement control) and torsional (load control) loading is derived as follows. For rotational control (the applied rotation, θ, is held fixed during crack propagation), we have

$$\Pi = U - W, \quad U = \frac{1}{2}T\theta \quad \text{and} \quad W = 0$$

$$\mathscr{G} = \frac{\theta}{8\pi r_0}\frac{\mathrm{d}T}{\mathrm{d}l}$$

Using the definition of compliance $c = r_0\theta/T$, we get

$$\mathscr{G} = \frac{T^2}{8\pi r_0^2}\frac{\mathrm{d}c}{\mathrm{d}l} \tag{11}$$

For torque control (the applied torque, T, is held fixed during crack propagation), the expressions are

$$\Pi = U - W, \quad U = \frac{1}{2}T\theta \quad \text{and} \quad W = T\theta$$

$$\mathscr{G} = \frac{T}{8\pi r_0}\frac{\mathrm{d}\theta}{\mathrm{d}l}$$

Using the definition of compliance, $c = r_0\theta/T$, we get

$$\mathscr{G} = \frac{T^2}{8\pi r_0^2}\frac{\mathrm{d}c}{\mathrm{d}l} \tag{12}$$

The expression for $\mathrm{d}c/\mathrm{d}l$ for a solid circular cylinder of length $2l$ and made of linear elastic material is $2/(GJ)$, where G is the shear modulus of the material and J, is the polar moment of inertia given by $\pi r_0^4/2$. Hence, we can write the expression for strain energy release rate as follows

$$\mathscr{G} = \frac{T^2}{4\pi r_0^2 GJ}$$

When the strain energy release rate becomes equal to $2\gamma_\mathrm{f}$ the crack will propagate leading to failure. The critical failure stress in torsion can then be written in terms of γ_f as follows.

$$\tau_\mathrm{cr} = 4\sqrt{\gamma_\mathrm{f} G/r_0} \tag{13}$$

For a non-linear elastic material, the expression for strain energy release rate, $\mathscr{G}$ (we continue with the notation $\mathscr{G}$ even though J is standard notation for non-linear materials), can be obtained as follows. For displacement control (the applied rotation, θ, is held fixed during crack propagation)

$$\begin{aligned} &\Pi = U - W \\ &U = \int_V \int_0^\gamma \tau(\zeta)\,\mathrm{d}\zeta\,\mathrm{d}V = 4\pi l \int_0^{r_1}\int_0^\gamma \tau(\zeta)\,\mathrm{d}\zeta r\,\mathrm{d}r \\ &W = 0 \end{aligned} \tag{14}$$

$$\mathscr{G} = -\frac{\mathrm{d}\Pi}{\mathrm{d}A} = -\frac{1}{4\pi r_0}\frac{\mathrm{d}U}{\mathrm{d}l} \tag{15}$$

In Eq. (14), the inner integral is a known function of ζ, where ζ is a dummy variable for the purpose of integration. But, the outer integral in r has to be first converted in terms of shearing strain γ since for a solid cylinder we do not know the distribution of τ with respect to the radius of cylinder, r. Using the relations $\gamma = rv$, and $\mathrm{d}r = \mathrm{d}\gamma/v$, in the integral of Eq. (14) we get the following integral. Here, v is the twist per unit length given by the ratio θ/l

$$U(\gamma) = 4\pi l \int_0^{\gamma_{r_1}} \left[\int_0^\gamma \tau(\zeta)\,\mathrm{d}\zeta\right]\gamma/v^2\,\mathrm{d}\gamma \tag{16}$$

Differentiating Eq. (16) with respect to l we get

$$\frac{\mathrm{d}U}{\mathrm{d}l} = 4\pi \int_0^{\gamma_{r_1}} \left[\int_0^\gamma \tau(\zeta)\,\mathrm{d}\zeta\right]\gamma/v^2\,\mathrm{d}\gamma \tag{17}$$

where ζ is a dummy variable and γ_{r_1} is shear strain at radius, r_1.

3.2.5. Combined compression–torsion loading

Consider a concentric cylinder of fiber and matrix with a debond of length $2l$ as shown in Fig. 16. We can divide this RVE into a cracked region of linear elastic fiber and a non-linear elastic matrix and an uncracked region of non-linear elastic composite. Now let this RVE be subjected to a combined set of axial and torsional loads as shown in Fig. 16. P is the axial compressive load and T is the torsional load. The total strain energy release rate under combined compression–torsion loading can be written as the sum of axial and torsional strain energy release rate contributions. It should be noted that we are implicitly assuming that the non-linear torsional response is unaffected by the presence of axial stress. In Appendix B, we have described an analysis where the matrix and thus, the composite is treated as a deformation theory of plasticity solid. It turns out that the interaction effects (between axial stress and shear stress) are negligible and the problem can be addressed by appealing to superposition where the total energy release rate contribution is computed as the sum of $\mathscr{G}_{\text{axial}}$ and $\mathscr{G}_{\text{torsion}}$, with each of their contributions computed with an assumption of non-interaction between axial stress and shear stress. Thus

$$\mathscr{G}_{\text{total}} = \mathscr{G}_{\text{axial}} + \mathscr{G}_{\text{torsion}} \tag{18}$$

In the present case, it was observed during the experiments that the axial stress–strain curve remains linear up to the point of failure even under combined compression–torsion loading. Hence, strain energy release rate, $\mathscr{G}_{\text{axial}}$ is obtained based on linear elastic material behavior. In torsion, the strain energy release rate, $\mathscr{G}_{\text{torsion}}$, is obtained by adding the strain energy release rate contributions from a linear elastic fiber and non-linearly elastic matrix in the cracked region and a non-linearly elastic composite in the uncracked region under torsional load.

$$\mathscr{G}_{\text{torsion}} = -\frac{1}{4\pi r_0}\frac{\mathrm{d}U}{\mathrm{d}l} = -\frac{1}{4\pi r_0}\left[\underbrace{\frac{\mathrm{d}U}{\mathrm{d}l_{\text{ fiber}}} + \frac{\mathrm{d}U}{\mathrm{d}l_{\text{ matrix}}}}_{\text{cracked region}} + \underbrace{\frac{\mathrm{d}U}{\mathrm{d}l_{\text{ composite}}}}_{\text{uncracked region}}\right] \tag{19}$$

Now, explicit relations for the terms entering in Eq. (19) are given below for both the cracked region and the uncracked region. In the cracked region the fiber is assumed to be linear elastic hence the term $\mathrm{d}U/\mathrm{d}l_{\text{fiber}}$ can be written as

$$\frac{\mathrm{d}U}{\mathrm{d}l_{\text{ fiber}}} = \frac{\tau^2\pi^2 r_0^2}{2G_{\text{fiber}}} \tag{20}$$

Also, in the cracked region, the matrix is debonded from the fiber and is modeled as a non-linear elastic material for the calculation of $\mathrm{d}U/\mathrm{d}l_{\text{matrix}}$.

Matrix

$$\frac{\mathrm{d}U}{\mathrm{d}l_{\text{ matrix}}} = 4\pi\int_{\gamma_{r_0}}^{\gamma_{r_1}}\left(\int_0^{\gamma}\tau_{\mathrm{m}}(\zeta)\,\mathrm{d}\zeta\right)\gamma/v^2\,\mathrm{d}\gamma \tag{21}$$

Uncracked region. In the uncracked region away from the crack tip we model the composite as a homogeneous non-linear elastic material. Thus, the expression for $\mathrm{d}U/\mathrm{d}l_{\text{composite}}$ can be written as follows:

Composite

$$\frac{\mathrm{d}U}{\mathrm{d}l_{\text{ composite}}} = 4\pi\int_0^{\gamma_{r_1}}\left(\int_0^{\gamma}\tau_{\mathrm{c}}(\zeta)\,\mathrm{d}\zeta\right)\gamma/v^2\,\mathrm{d}\gamma \tag{22}$$

From Eqs. (10), (20)–(22), we can write an expression for the total strain energy release rate (SERR) of the composite as

$$\mathscr{G}_{\text{Total}} = \frac{\sigma_c^2 r_0}{4V_f^2}\left(\frac{1}{\delta}-\beta\right) + \frac{\tau^2\pi^2 r_0^2}{2G_{\text{fiber}}} + \frac{1}{r_0}\int_{\gamma_{r_0}}^{\gamma_{r_1}}\left(\int_0^{\gamma}\tau_m(\zeta)\,d\zeta\right)\gamma/v^2\,d\gamma + \frac{1}{r_0}\int_0^{\gamma_{r_1}}\left(\int_0^{\gamma}\tau_c(\zeta)\,d\zeta\right)\gamma/v^2\,d\gamma \quad (23)$$

When the total strain energy release rate, $\mathscr{G}_{\text{Total}}$ becomes equal to $2\gamma_f$, then splitting failure occurs. Therefore, we can write the above equation for compression strength, σ_c, under combined loading as

$$\gamma_f = \frac{\sigma_c^2 r_0}{8V_f^2}\left(\frac{1}{\delta}-\beta\right) + \frac{\tau^2\pi^2 r_0^2}{4G_{\text{fiber}}} + \frac{1}{2r_0}\int_{\gamma_{r_0}}^{\gamma_{r_1}}\left(\int_0^{\gamma}\tau_m(\zeta)\,d\zeta\right)\gamma/v^2\,d\gamma + \frac{1}{2r_0}\int_0^{\gamma_{r_1}}\left(\int_0^{\gamma}\tau_c(\zeta)\,d\zeta\right)\gamma/v^2\,d\gamma \quad (24)$$

4. Solution procedure

Eq. (24) relating γ_f to the axial stress and shear stress acting on the composite is solved numerically to obtain the critical value of compressive stress and the corresponding value of shear stress. The input parameters required to solve Eq. (24) are the elastic and geometric properties of fiber, the complete nonlinear shear response of the pure matrix and the complete nonlinear shear response of the composite and the fiber volume fraction of the composite. Table 1 shows the properties used in the present failure model. The shear responses were incorporated in the analytical solution by using the Ramberg–Osgood fit parameters obtained from Yerramalli and Waas (2002b) and are given in Table 2. With the above input parameters, the equation is solved for the critical value of shear stress or compressive stress for different values of loading ratios, κ, where κ is defined as σ/τ. The critical value of shear stress or compressive stress is attained when for a particular value of κ, the right-hand side of Eq. (23) exceeds the left-hand side value of critical fracture energy, γ_f. A range of γ_f values of 0.1224–0.0408 kJ/m^2 has been used to study the effect of fracture energy on the predicted failure envelope.

5. Discussion

As has been discussed in the experimental results section, the combined axial compression–torsion loading of solid circular cylindrical specimens of glass/vinylester and carbon/vinylester composites indicated that the remotely applied shear stress caused a degradation in the composite compressive behavior leading to a decrease in the failure strength. However, there was a difference in the response of carbon composites to remote shear stress as compared to that of glass composites. The carbon composites show a nearly linear reduction in compressive strength as the remote shear stress is increased, which matches with the prediction

Table 1
Properties of glass fiber and vinylester resin

	E_f (MPa)	μ_f (MPa)	r_0 (mm)
Glass fiber	72000	29508	0.012
Vinylester	3585	1318	

Table 2
Ramberg–Osgood fit for shear stress–strain curve of glass/vinylester and pure vinylester specimens

	V_f	μ_c (MPa)	A	n
Glass composite	0.5	3260	68.68	12.44
Vinylester	0	1318	65.44	7.9603

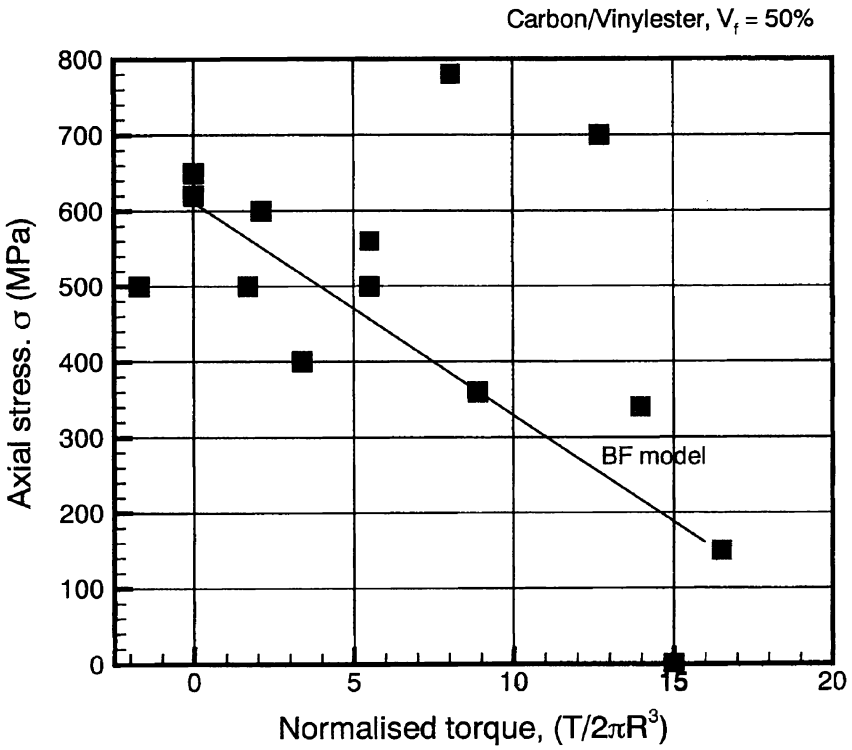

Fig. 18. Combined compression–torsion failure plot for carbon/vinylester composite of $V_f = 50\%$.

of the MBF model, Eq. (5). This can be observed in Fig. 18, where the axial compressive strength is plotted against a normalized torque defined as $\frac{T}{2\pi R^3}$. On the other hand, the glass/vinylester composites were found to be initially unaffected by the remotely applied shear stress. When the remote shear stress has exceeded a critical value, a drop in compressive strength was observed as can be seen in Fig. 19.

The results in Fig. 19 indicate that the MBF kinking model predictions (with $\Phi = 4$ deg) are inaccurate for the glass composites which were tested under combined compression–torsion loading. It is noted that for $\Phi = 2$ deg, the MBF prediction become higher but the trend is still inconsistent with the experimental data. This is because the glass composites tested fail by splitting as observed in experiments, instead of failing in a kinking mode. This observation indicates the need for a model that explicitly accounts for the effect of fiber properties and the fiber/matrix interfacial fracture energy on the composite compressive strength. The current fracture mechanics based model is used to compare the predicted and the observed experimental values for the failure envelope under a combined state of compression–torsion loading. The value of fracture energy as a function of fiber volume fraction of the composite is not available but a initial value of $\gamma_f = 0.1224$ kJ/m^2 has been chosen to predict the failure envelope. The failure envelope predictions based on this value of γ_f are very high since this value of γ_f corresponds to the fracture energy of pure epoxy and is more suitable for lower volume fractions. Also, the failure of glass composites at high volume fractions was seen to be a combination of splitting and kinking. Hence, the failure model was used to predict the failure envelope for a range of fracture energy ($\gamma_f = 0.1224$ kJ/m^2, $\gamma_f = 0.0612$ kJ/m^2, $\gamma_f = 0.0408$ kJ/m^2). The correlation between the predicted stresses and the experimentally obtained data is good as indicated in Fig. 20. The better correlation between the predicted value of compressive strength and experimentally observed strength for a lower value of γ_f could indicate that the interfacial fracture energy

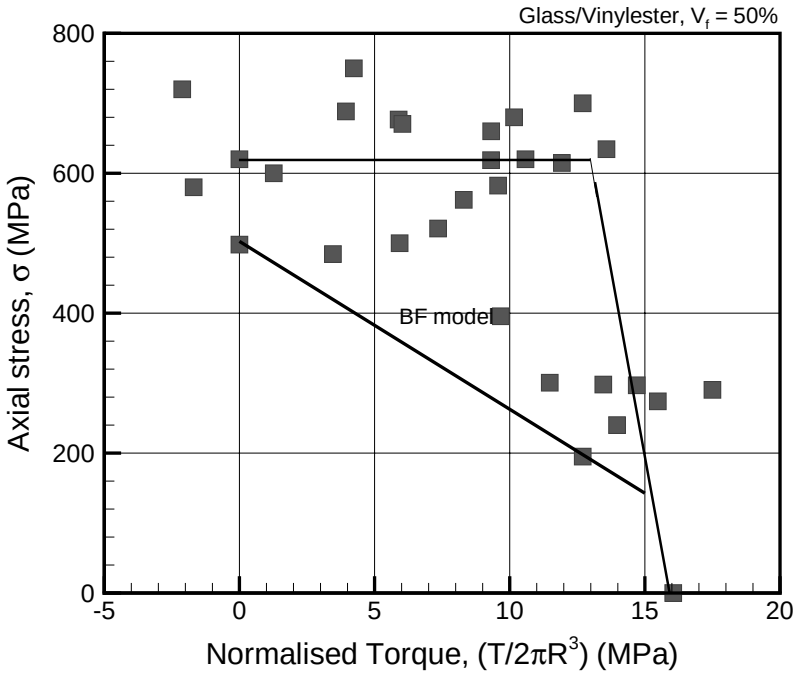

Fig. 19. Combined compression–torsion failure plot for glass/vinylester composite of $V_f = 50\%$.

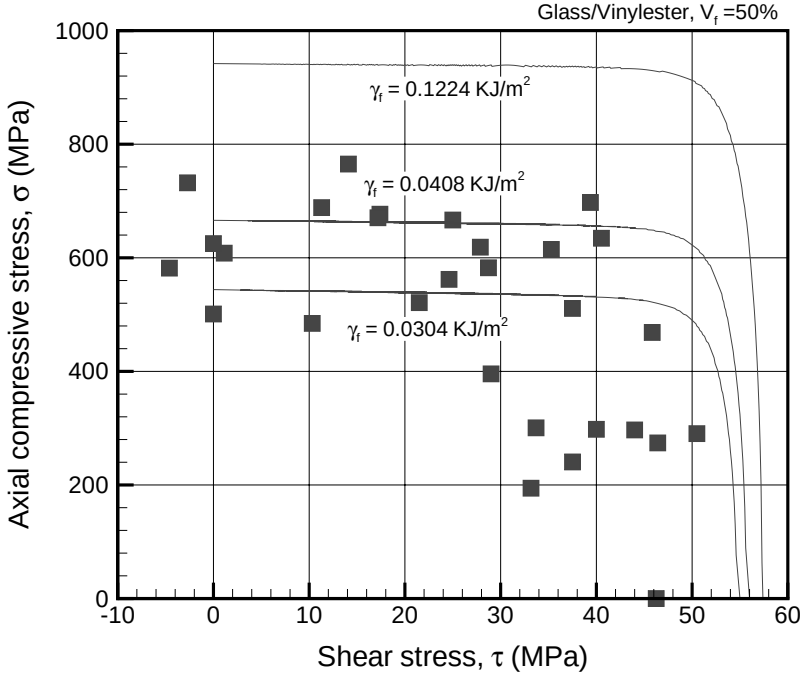

Fig. 20. Comparison of the new fracture critieria with experimental data for a glass/vinylester composite of $V_f = 50\%$.

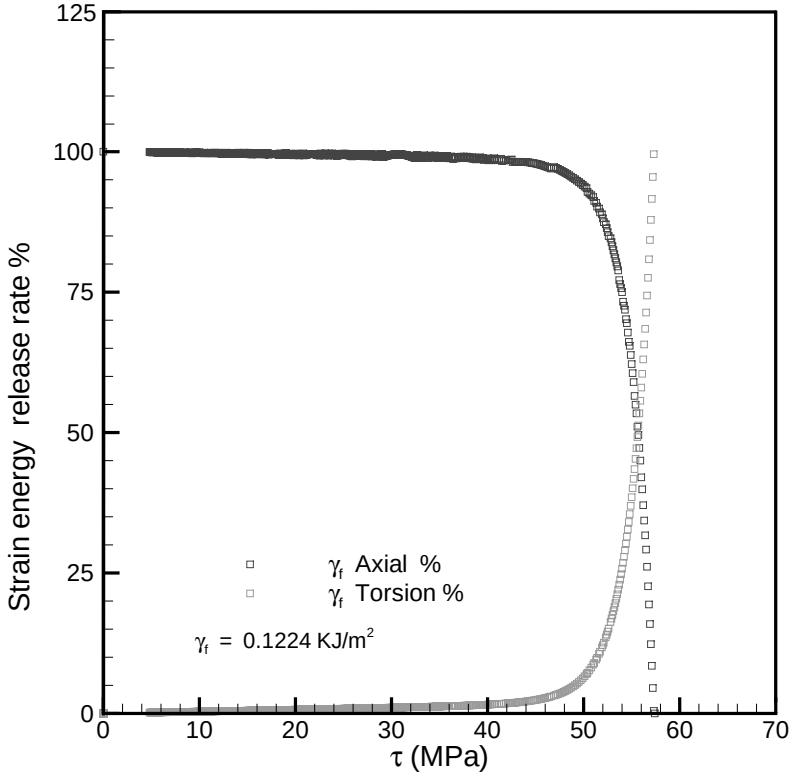

Fig. 21. Variation of axial and torsional SERR with shear stress, τ for glass/vinylester composite of $V_f = 50\%$.

reduces at higher fiber volume fraction. The new model captures the trend of the failure data and the correlation is much better in the range where the loading ratio, κ is high. At lower values of κ the model predicts higher values of compressive strength than the observed experimental values. However, it should be noted that the failure mode in case of higher values of shear stress (i.e. lower κ) was not pure splitting but a combination of matrix crushing and splitting, which is not taken into account by the current splitting fracture model. To better understand the initial insensitivity of the glass composites to remote shear stress, a plot of axial strain energy release rate (SERR) and torsional SERR as a precentage of the total SERR with respect to the applied shear stress, τ, is shown in Fig. 21. It can be seen from Fig. 21 that up to a significant value of remote shear stress, τ, the axial SERR contribution to the total SERR is nearly 100% indicating that remotely applied shear stress does not play a role in inducing failure as seen in experiments. When the shear stress τ reaches a critical value, which is about 40–50 MPa for the glass composites there is a sudden rise in the contribution from the torsional SERR and it reaches a peak value of 100% for pure torsion loading.

6. Conclusions

Motivated by the experimental results obtained, we have presented a new fracture mechanics based model to predict splitting failure in unidirectional composites subjected to remote combined axial compression and torsional loading. Experimentally it was found that the response mechanism of glass fiber

composites to remote shear stress is different from that of the carbon fiber composites. The results indicate that the conventional Budiansky–Fleck model is applicable to carbon fiber composites, where the failure is due to buckling of fibers in an inelastic matrix. In glass composites there seems to be a critical value of remote shear stress beyond which the compressive strength of the composite degrades very rapidly. This difference in sensitivity to the remote shear stress led us to develop a new fracture mechanics based failure model which captures the initial insensitivity of compressive strength to shear stress and the subsequent steep drop in compressive strength when the remotely applied shear stress is very high. Apart from the difference in sensitivity to remote shear stress exhibited by carbon and glass composites, the failure mechanism is also found to be different. In glass composites the failure mechanism changed from splitting to kinking. A combination of matrix crushing and splitting was observed as the remote shear stress was increased. A single model which can effectively tackle the mode transition from splitting to kinking failure and vice-versa would be ideal. Conceivably, such a model would have to be implemented numerically, perhaps using the finite element method.

Acknowledgements

The authors are grateful to the Army Research Office for supporting this research. Dr. Bruce LaMattina is the ARO scientific monitor.

Appendix A. Axial compliance of a misaligned fiber

Consider the response of an axially loaded misaligned fiber of uniform cross-sectional area, A_f, length $2l$ and elastic modulus E_f within the context of geometrically nonlinear Euler–Bernoulii beam theory in the X–Z plane. Let a set of cartesian coordinate axes be chosen such that the X-axis is pointing along the center line of the fiber and Z-axis is pointing in a direction transverse to the X-axis. Let the origin of the axes be such that $x = 0$ is at the center and $x = \pm l$ signify the abcissae of the crack tips. Let the initial misalignment, total deflection in the Z-direction measured from the fiber centerline and the additional deflection be denoted by $w_0(x)$, $w(x)$ and $w_1(x)$, respectively. Then, the deflection, $w(x) = w_0(x) + w_1(x)$, is governed by

$$\frac{d^4 w}{dx^4} - \frac{d^4 w_0}{dx^4} + \lambda^2 \frac{d^2 w}{dx^2} = 0$$

where $\lambda^2 = \frac{P_f}{E_f I_f}$. Assuming an initial misalignment distribution of $w_0(x) = A_0(1 + \cos\frac{\pi x}{l})$, solving the above equation for clamped boundary conditions at $x = \pm l$, and, adopting the definition of axial strain $\epsilon_x = \frac{du}{dx} + \frac{1}{2}\left(\frac{dw}{dx}\right)^2 - \frac{1}{2}\left(\frac{dw_0}{dx}\right)^2$, in conjunction with the one dimensional stress-strain relation $\sigma_x = E_f \epsilon_x$, we obtain the relation,

$$(EA)_{\text{eff}} = \frac{E_f A_f}{1 + \frac{A_0^2 A_f}{2I_f}}$$

Appendix B. Interaction between the axial stress and torsional stress

In this section, the effect of axial stress on the non-linear behavior of the matrix and composite under shear stress is studied. For this purpose we use a $J2$ deformation theory of plasticity to model the matrix and the composite material. The general method is described as follows. We first model the material as a non-linear material and use a Ramberg–Osgood fit of the form $\gamma = (\tau/G) + (\tau/A)^n$ to describe the behavior of the material in shear. Then using the definition of equivalent stress and equivalent strain, we can get the

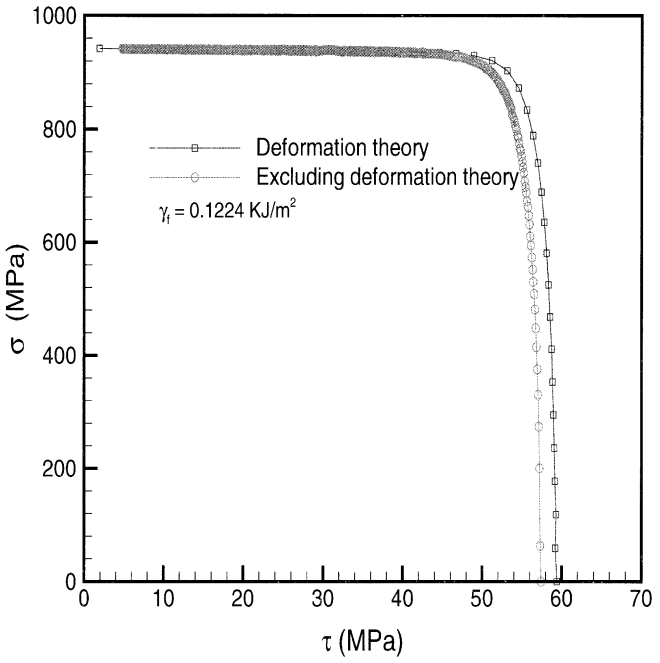

Fig. 22. Comparison of failure envelopes considering the composite as a deformation theory solid and as a nonlinear elastic solid.

stress–strain curve of the material under uniaxial load. The uniaxial stress–strain relation is obtained in the form $\epsilon = (\sigma/\epsilon) + (\sigma/B)^n$, where $B = A3(1/2 + 1/2n)$. Once the uniaxial stress–strain curve is determined we can determine the plastic secant modulus, E_s^p and the Poisson's ratio as follows

$$E_s^p = \frac{B^n E}{B^n + E\sigma^{n-1}}$$

$$v_s = \frac{1}{2} + \frac{E_s^p(v - 1/2)}{E}$$

Once the secant modulus and Poisson's ratio are determined, then the corresponding shear stress and the shear strain can be determined. Fig. 22 shows a comparison between the failure envelope predicted by considering the material as a deformation theory of plasticity solid and the one obtained by not assuming it to be a deformation theory of plasticity solid. It can be seen that there is not much of a difference between the two curves except in the range where the compressive stress is low and shear stress is high.

References

Argon, A.S., 1972. Fracture of composites. In: Herman, H. (Ed.), Treatise on Materials Science and Technology, vol. 1. Academic Press, New York, pp. 79–114.

Budiansky, B., 1983. Micromechanics. Computers and Structures 16, 3–12.

Budiansky, B., Fleck, N.A., 1993. Compressive failure of fibre composites. Journal of the Mechanics and Physics of Solids 41 (1), 183–211.

Christensen, R.M., 1991. Mechanics of Composite Materials, first ed. Krieger Publishing Company, Malabar, FL.

Drapier, S., Grandidier, J.-C., Potier-Ferry, M., 2001. A structural approach of plastic microbuckling in long fibre composites: comparison with theoretical and experimental results. International Journal of Solids and Structures 38 (22–23), 3877–3904.

Fleck, N.A., 1997. Compressive failure of fiber composites. In: Advances in Applied Mechanics, vol. 33. Academic Press, New York, pp. 43–117.

Fleck, N.A., Deng, L., Budiansky, B., 1995. Prediction of kink width in compressed fiber composites. ASME Journal of Applied Mechanics 62, 329–337.

Horii, H., Nemat-Nasser, S., 1985. Compression-induced microcrack growth in brittle solids: axial splitting and shear failure. Journal of Geophysical Research 90 (B4), 3105–3125.

Horii, H., Nemat-Nasser, S., 1986. Brittle failure in compression: splitting, faulting, and brittle–ductile transition. Philosophical Transactions of the Royal Society of London, Series-A Physical Sciences and Engineering 319, 337–374.

Hsu, S.Y., Vogler, T.J., Kyriakides, S., 1999. Inelastic behavior of an as4/peek composite under combined transverse compression and shear. Part II: modeling. International Journal of Plasticity 15, 807–836.

Hyer, M.W., Waas, A.M., 2000. Mircomechanics of linear elastic continuous fiber composites. In: Chou, T.W. (Ed.), Comprehensive Composite Materials, vol. 1. Elsevier Science, Amsterdam, Chapter 12.

Jelf, P.M., Fleck, N.A., 1994. The failure of composite tubes due to combined compression and torsion. Journal of Material Science 29, 3080–3084.

Kyriakides, S., Arseculeratne, R., Perry, E.J., Liechti, K.M., 1995. On the compressive failure of fiber reinforced composites. In: Proceedings of the Sixtieth Birthday Celebration of Prof. W.G. Knauss. International Journal of Solids and Structures. 32, 689–738.

Lee, S.H., Waas, A.M., 1999. Compressive response and failure of fiber reinforced unidirectional composites. International Journal of Fracture 100, 275–306.

Lyon, R.E., 1991. Shear strength of a ductile material from torsion test of solid cylinders. Journal of Testing and Evaluation 19 (3), 240–243.

Martinez, G.M., Piggott, M.R., Bainbridge, D.M.R., Harris, B., 1981. The compression strength of composites with kinked, misaligned and poorly adhering fibres. Journal of Materials Science 16, 2831–2836.

Nadai, A., 1950. In: Theory of Flow and Fracture of Solids, vol. 1. Mc-Graw Hill, New York.

Naik, N.K., Kumar, R.S., 1999. Compressive strength of unidirectional composites: evaluation and comparison of prediction models. Composite Structures 46, 299–308.

Narayanan, S., Schadler, L.S., 1999. Mechanisms of kink-band formation in graphite/epoxy composites: a micromechanical experimental study. Composite Science and Technology 59, 2201–2213.

Nemat-Nasser, S., Deng, H., 1994. Strain rate effect on brittle failure in compression. Acta Metallurgica Materialia 42 (3), 1013–1024.

Nemat-Nasser, S., Horii, H., 1982. Compression-induced nonplanar crack extension with application to splitting, exfoliation, and rockburst. Journal of Geophysical Research 87 (B8), 6805–6821.

Oguni, K., Ravichandran, G., 2000. An energy-based model of longitudinal splitting in unidirectional fiber-reinforced composites. Journal of Applied Mechanics 67, 437–443.

Piggott, M.R., 1981. A theoretical framework for the compressive properties of aligned fibre composites. Journal of Materials Science 16, 2837–2845.

Piggott, M.R., Harris, B., 1980. Compression strength of carbon, glass and kevlar-49 fibre reinforced polyester resins. Journal of Materials Science 15, 2523–2538.

Rosen, B.W., 1965. Mechanics of composite strengthening. In: Bush, S.H. (Ed.), Composite Materials. American Society of Metals, Metals Park, OH, pp. 37–75.

Vogler, T.J., Hsu, S.Y., Kyriakides, S., 2000. Composite failure under combined compression and shear. International Journal of Solids and Structures 37, 1765–1791.

Vogler, T.J., Kyriakides, S., 1999. Inelastic behavior of an as4/peek composite under combined transverse compression and shear. Part I: experiments. International Journal of Plasticity 15, 783–806.

Vogler, T.J., Kyriakides, S., 2001. On the initiation and growth of kink bands in fiber composites. Part I: experiments. International Journal of Solids and Structures 38, 2639–2651.

Waas, A.M., Schultheisz, C.R., 1996. Compressive failure of composites parts I and II. Progress in Aerospace Sciences 32 (1), 1–78.

Wisnom, M.R., Atkinson, J.W., 1997. Constrained buckling tests show increasing compressive strain to failure with increasing strain gradient. Composites-Part A: Applied Science and Manufacturing 28 (11), 959–964.

Yerramalli, C.S., Waas, A.M., 2002a. Compressive splitting failure of composites using modified shear lag theory. International Journal of Fracture 115 (May), 27–40.

Yerramalli, C.S., Waas, A.M., 2002b. In situ matrix shear response using torsional test data of fiber reinforced unidirectional polymer composites. ASME Transactions of Journal of Engineering Materials and Technology 124 (April), 152–159.